

5. J.-Y. Kim and H. C. Hsieh, *J. Lightwave Technol.* **10**, 439 (1992).
6. G. Stemme, *J. Micromech. Microeng.* **1**, 113 (1991).
7. K. Hane and S. Hattori, *Appl. Opt.* **29**, 145 (1990).
8. H. Ukita, Y. Katagiri, Y. Uenishi, *Jpn. J. Appl. Phys.* **26** (suppl. 26-4), 111 (1987).
9. F. Shimokawa, H. Tanaka, Y. Uenishi, R. Sawada, *J. Appl. Phys.* **66**, 2613 (1989).
10. Z. L. Zhang, G. A. Porkolab, N. C. MacDonald, in *Proceedings of IEEE Micro Electro Mechanical System '92*, W. Benecke and H.-C. Petzold, Eds. (Travemünde, Germany, 4 to 7 February 1992) (IEEE, New York, 1992), p. 72.
11. H. Muro and S. Hoshino, *Trans. Inst. Electron. Inf. Commun. Eng. J74-C-II*, 421 (1991) (in Japanese).
12. M. Tabib-Azar and J. S. Leave, *Sensors Actuators*, **A21-23**, 229 (1990).
13. D. Walsh and B. Culshaw, *ibid.* **A25-27**, 711 (1991).
14. We thank K. Itao and E. S. Vera for helpful discussions.

29 September 1992; accepted 2 February 1993

X-ray Tomographic Study of Chemical Vapor Infiltration Processing of Ceramic Composites

J. H. Kinney, T. M. Breunig, T. L. Starr, D. Haupt, M. C. Nichols, S. R. Stock, M. D. Butts, R. A. Saroyan

The fabrication of improved ceramic-matrix composites will require a better understanding of processing variables and how they control the development of the composite microstructure. Noninvasive, high-resolution methods of x-ray tomography have been used to measure the growth of silicon carbide in a woven Nicalon-fiber composite during chemical vapor infiltration. The high spatial resolution allows one to measure the densification within individual fiber tows and to follow the closure of macroscopic pores in situ. The experiments provide a direct test of a recently proposed model that describes how the surface area available for matrix deposition changes during infiltration. The measurements indicate that this surface area is independent of the fiber architecture and location within the preform and is dominated by large-scale macroporosity during the final stages of composite consolidation. The measured surface areas are in good agreement with the theoretical model.

High fracture toughness and strength give ceramic-matrix composites an advantage over monolithic ceramics. Ceramic-matrix composites, particularly those based on silicon carbide (SiC), can withstand high temperatures and corrosive environments. Accordingly, their use is beginning to be considered necessary in advanced aircraft engine structures and heat management applications. Before these materials can fulfill their potential, however, their fabrication costs must be reduced greatly and their mechanical properties must be improved. Improvements in mechanical properties will come about largely through reduced and controlled residual porosity, which will require better understanding of processing variables and how they ultimately relate to the composite microstructure.

Chemical vapor infiltration (CVI) is an important technology for the fabrication of SiC ceramic-matrix composites (1). In CVI, a vapor precursor of the matrix material, methyltrichlorosilane (MTS), is passed through a network of reinforcing fibers at elevated temperature. The MTS dissociates, and the SiC matrix phase deposits on the

fibers. As matrix growth progresses, avenues for gas transport become more constricted and begin to close off, eventually stopping the infiltration process. Pore closure determines the final density of the composite.

The manufacture of woven-fiber, ceramic-matrix composites is, in some ways, similar to the technology of textile weaving. Thin (diameters of 10 to 20 μm) fibers are combined into bundles (tows) and are woven into cloth. The cloth layers are formed into a nearly final shape called a preform, which is then infiltrated with MTS. The architecture of the cloth (that is, the geometry of the weave) can be as simple as a square, two-dimensional weave or as complicated as a three-dimensional (3D) weave. In the lay-up of the cloth, the tow directions may be identical between layers (a $0^\circ/90^\circ$ architecture) or they may be rotated between layers (for example, a $0^\circ/45^\circ$ or $0^\circ/30^\circ/60^\circ$ architecture). The architecture determines the directionality of the mechanical properties and may affect the infiltration behavior.

In the woven structure are two distinct classes of porosity. The voids within the fiber tows are called micropores, and the separations between cloth layers (channels) and the interstices that form between the intersecting tows in the cloth (holes) are called macropores. The channels and holes are the primary avenues for vapor transport

through the preform; hence, infiltration-induced changes in the macropore dimensions will greatly affect vapor flow and composite consolidation.

In addition to the effects of the macropores on vapor flow, the rate at which the matrix phase grows is strongly influenced by the reaction rates and by the amount of surface area available for deposition. The reaction rates for MTS decomposition and SiC growth have been reported (2). The surface area, however, depends on the microstructure of the composite. Because of the small surface areas of both micro- and macropores ($<<500 \text{ cm}^2 \text{ g}^{-1}$), independent measurements of the surface area during infiltration cannot be made with traditional techniques such as Brunauer, Emmett, Teller gas adsorption or Hg porosimetry, which both require larger surface areas (3). Prior attempts at metallurgical sectioning and stereological measurements have been inconclusive, primarily because the small number of pores, coupled with strong anisotropy, requires an inordinate number of sections to obtain good statistics (4).

A model of surface area (the uniform deposition model) has recently been proposed to describe the CVI process in the woven architecture of continuous fiber composites (5). This model assumes that the fiber tows occupy 70% of the total volume and that they are $\sim 40\%$ porous [the remaining space is occupied by channel porosity (25%) and hole porosity (5%)]. Before infiltration, the majority of the available surface area is within the tows. As infiltration proceeds, the small pores within the tows fill in rapidly, and the surface area decreases dramatically. When the composite reaches a fractional density of $\sim 70\%$, the surface area becomes dominated by the macropores, which, because of their larger size, fill in more slowly. The last 30% of consolidation is financially costly because most of the infiltration time is expended during this phase.

To test the validity of the uniform deposition model and to quantify the changes in surface area occurring during infiltration, we have used a noninvasive volume-imaging technique to analyze the microstructure and macrostructure of a woven-fiber composite. Carlson and Denison demonstrated that x-ray microtomography is an effective technique for providing statistically valid microstructural information when conventional sectioning fails to do so (6). However, the spatial resolution of the industrial microtomography system (150 μm) used in their experiment is not adequate to provide accurate measurements of the surface area of continuous fiber composites.

New approaches to high-resolution x-ray tomography with solid-state detectors and monochromatic synchrotron radiation pro-

J. H. Kinney, D. Haupt, R. A. Saroyan, Lawrence Livermore National Laboratory, Livermore, CA 94551. T. M. Breunig and M. C. Nichols, Sandia National Laboratories, Livermore, CA 94550. T. L. Starr, S. R. Stock, M. D. Butts, Georgia Institute of Technology, Atlanta, GA 30332.

vide much higher spatial resolution than do industrial microtomography systems (7, 8). The spatial resolution of the x-ray tomographic microscope (XTM), for example, can be adjusted between 1 and 20 μm . This range is sufficient to image microstructural features in complicated woven-fiber architectures (9). The XTM provides a volume resolution that is more than three orders of magnitude finer than that reported for industrial tomography systems. With the XTM, therefore, it is possible to make noninvasive, 3D images of pores and fibers in a composite preform. The nondestructive nature of the XTM allows quantitative measurements of microstructural evolution to be obtained as infiltration proceeds. The problems associated with the small (<1 mm) sample sizes required in previous XTM systems have been overcome by recent improvements to the instrument. The sample size that can be imaged at high resolution has been significantly increased, allowing realistic CVI specimens to be studied (10).

For our experiments here, we used the XTM to measure the local average surface area as a function of local average fractional density in a woven Nicalon (amorphous SiC; Nippon Carbon) fiber-reinforced composite. Each tow in the composite contained ~ 500 Nicalon fibers. Both $0^\circ/90^\circ$ and $0^\circ/45^\circ$ plane-weave architectures were studied. We made preforms, each 6.2 mm in diameter and 6.0 mm high, by stacking 20 layers of Nicalon cloth into a cylindrical graphite reaction chamber. This chamber could be inserted and removed from a furnace maintained at 975°C . Reactant gas, consisting of H_2 bubbled through liquid MTS at laboratory ambient temperature, was forced through the graphite tube and fiber preform (isothermal, forced-flow CVI). The excess H_2 and reaction by-products exited through the gas outlet.

Three-dimensional images of the fiber preforms in the reaction chambers were made before infiltration (11). Densification was then followed as a function of infiltration time by interruptions in the processing of these samples at various stages. After each stage, the XTM was used to provide 3D images of the samples. The volume elements (voxels) used to create the microstructural images were $15.8 \mu\text{m}$ in all three dimensions. Although a $15.8\text{-}\mu\text{m}$ voxel is the same size as the micropores in the preform, the volume fraction of Nicalon fibers (and hence the pore fraction) within the tow could still be determined with good precision by determination of averages over several volume elements in the tow (for example, 5 by 5 by 5 supervoxels). In the preform, initially a two-phase mixture of fibers and pores, the fiber fraction in a tow, V_v^N , can be determined from the XTM data with the relation

$$V_v^N = \frac{\langle \alpha \rangle}{\mu_N \rho_N} \quad (1)$$

where $\langle \alpha \rangle$ is the measured linear attenuation coefficient for the voxel, μ_N (in square centimeters per gram) is the mass attenuation coefficient for Nicalon at the x-ray energy that is used to create the image, and ρ_N is the density of a Nicalon fiber (12). Using this relation, we determined the volume fraction of Nicalon fibers at the center of the tows at 264 different locations within the preform. The results indicated that this volume fraction was 0.55 ± 0.02 , in agreement with optical microscopy values on sections of nearly identical samples taken after they were processed (0.56 ± 0.07) (13). With the XTM, we measured the total volume fraction of fibers in the composite as 0.35, which compares favorably to an estimate of 0.38, on the basis of packing density of tows in the preform.

Once we established the volume fraction of Nicalon fibers in the preform tows, we could follow the densification of the tows during subsequent infiltration. The fractional density of the tows is given by

$$\rho_T = V_v^N + V_v^{\text{SiC}} \quad (2)$$

where

$$V_v^{\text{SiC}} = \frac{\langle \alpha \rangle - \langle \alpha' \rangle}{\mu_{\text{SiC}} \rho_{\text{SiC}}} \quad (3)$$

and $\langle \alpha \rangle - \langle \alpha' \rangle$ is the difference between the XTM measurements of the infiltrated sample and those of the preform. This relation is valid only when measurements are made at the same position within the sample during the course of the infiltration.

Figure 1 is a bar chart showing the measured micropore volume fractions ($1 - \rho_T$) obtained in the tows that were at

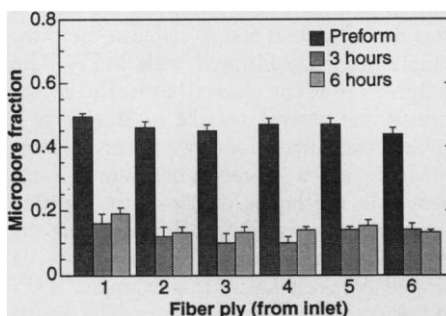


Fig. 1. Measurements by XTM of the micropore volume fraction within the tows of a $0^\circ/90^\circ$ fiber architecture as a function of infiltration time and distance from the vapor inlet. The dark bars are the volume fractions in the preform before infiltration. The dark gray and light gray bars are the volume fractions after 3 and 6 hours of infiltration, respectively. No statistical difference in pore density is observed between 3 and 6 hours of infiltration, indicating that the tows have become fully consolidated at the earliest stage of infiltration.

random sites within single fiber layers of a $0^\circ/90^\circ$ preform. The layers are numbered consecutively downstream from the gas inlet. The pore fractions measured in the uninfiltrated preform show little variation from the sample mean (0.45). However, after 3 hours of infiltration the tows have partially filled. No significant consolidation is evident after an additional 3 hours of infiltration (within the 95% confidence limits, the volume fraction of SiC in each tow remains unchanged between 3 and 6 hours of infiltration). By taking the XTM measurements from the same sample, we were able to show that the remaining pores in the tows must have become sealed off from the gas flow in <3 hours. Rapid tow consolidation is required for the uniform deposition model to be valid.

The volume elements used in this study were too large to enable the surface areas of the micropores to be measured. However, the macropores were large enough for us to use the XTM to measure their surface areas. To find these values, we defined a threshold in which single voxels with a linear attenuation coefficient that was half that of the Nicalon fiber (half occupied) were identified as belonging to the surface. Voxels with attenuation coefficients greater than half this value were assigned to filled regions (Nicalon or SiC), and voxels with less than half this value were considered pores. This use of thresholds eliminated micropores $<45 \mu\text{m}$ in diameter from the calculations of surface area—effectively making the tows appear solid.

We imaged the entire preform volume, defined by a 6.2-mm diameter and a 6-mm height, with a surrounding reaction chamber using >400 contiguous slices that were $15.8 \mu\text{m}$ thick. Three-dimensional images, each containing between 150 million and 250 million voxels, were constructed by the stacking of these slices. Figure 2 shows a portion of a 3D XTM image of a partially

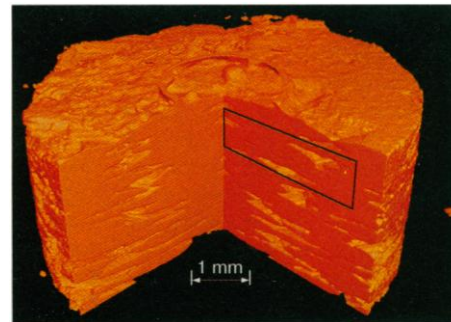


Fig. 2. Volume reconstruction by XTM of a $0^\circ/45^\circ$ preform after 3 hours of infiltration. A quarter wedge has been removed to reveal the channel and hole porosity that still remains after partial infiltration. This image has been obtained noninvasively, and the sample remains inside the reaction chamber.

infiltrated 0°/45° fiber preform. A higher magnification view is shown in Fig. 3A, which shows channel porosity intersecting the surface. By making the SiC matrix and Nicalon fibers slightly transparent (Fig. 3B), we can observe the interconnected network of pores. Visible in this view are both the holes (which connect the different layers vertically) and the horizontal channels. A rendering that shows only the porosity (when all solid matter was made completely transparent) provides a detailed image of both the spatial orientation and the surface structure of the macroporosity (Fig. 3C).

We fitted isosurface contours from the center of each surface voxel in slice planes situated normal to the direction of vapor flow. These contours defined the surface of the deposition substrate. The ratio of the surface perimeter to the slice plane area was used to determine the ratio of surface to volume for each slice plane in the preform. We determined the fractional density within each slice plane from the ratio of voxels above the threshold to the total number of voxels in the slice. Because this procedure did not account for any contributions from the microporosity, the resulting estimate of

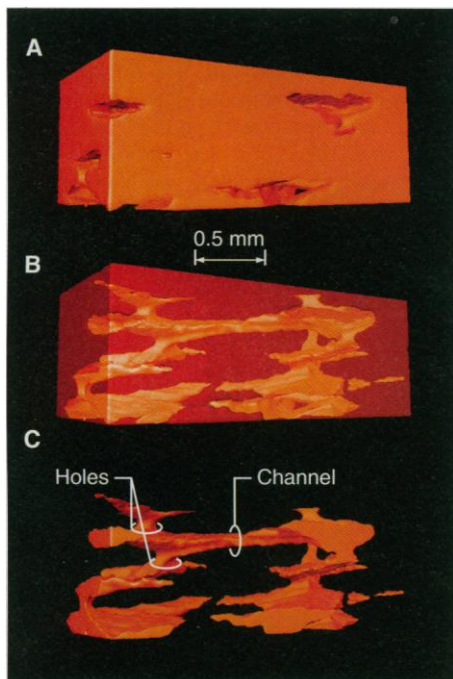


Fig. 3. Higher magnification view of the high-lighted region of the preform shown in Fig. 2. (A) Reconstruction by XTM showing channel porosity intersecting the surface. (B) Partial removal of the SiC matrix, revealing a complicated interconnected network of porosity. Visible are the holes, which connect the layers vertically, and the channels, which run horizontally. (C) Complete transparency of the matrix, revealing a more detailed view of the porosity within the sample.

surface area should match actual values only when fractional densities exceed 70% (that is, when macropores dominate). However, this range of densities defines the most important phase.

The deposition of matrix phase in isothermal, forced-flow CVI is greatest near the vapor inlet. This deposition leads initially to a gradient in fractional density between the inlet and the outlet. Because of this difference, conventional sectioning procedures would dictate that sections be made along the vapor flow direction normal to the cloth layers. The measurements along such a vertical sectioning plane should provide a mean surface area per sample volume that is averaged over widely varying fractional densities. What is important to this study, however, is a measure of the average local surface area as a function of the local average fractional density. Because the fractional density is most uniform in a horizontal (as opposed to vertical) plane, our method of using slice planes parallel to the fiber lay-up was necessary, although it departed from convention. Furthermore, any statistical problems that might be associated with the taking of sections perpendicular to a gradient during serial sectioning are eliminated because the XTM makes sections of each sample contiguously and in its entirety. This feature is a major advantage of tomographic methods for quantitative materials characterization.

Figure 4 shows the prediction of surface area per unit volume by the uniform deposition model for woven preforms and the experimentally determined values for both the 0°/45° and 0°/90° fiber architectures after 3 hours of infiltration. Experimental results are nearly identical after 6 hours of

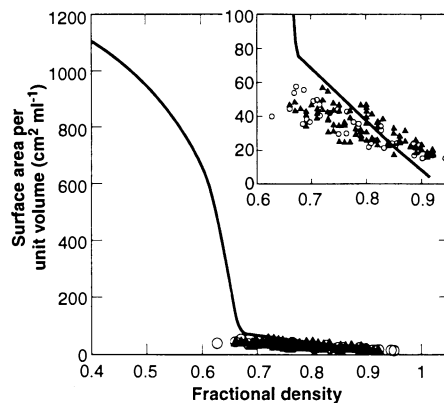


Fig. 4. Surface area per unit volume, as predicted by the uniform deposition model (solid line) and as measured with the XTM (circles and triangles). The inset provides greater detail of the surface area at fractional densities >0.7 . The open circles are the measured values for a 0°/90° preform after 3 hours of infiltration, and the solid triangles are the measured values for a 0°/45° preform after 3 hours of infiltration.

infiltration. The insert shows an expanded view of the predictions of the uniform deposition model compared with the data. The two sets of values are in good agreement between fractional densities of 0.7 and 1.0. Variations of the preform from the ideal architecture (packing defects) and nonuniform deposition within the individual plies cause scatter in the data. Nevertheless, no statistically significant differences exist between the measured surface areas for different two-dimensional fiber architectures.

These procedures provide a direct experimental test of the uniform deposition model. Part of the success of this model depends on the validated premise that the pores consolidate before the channels and holes have a chance to alter their morphology significantly. Even if tow interiors do not completely densify, the remaining microporosity is no longer surface connected; hence, the tows no longer affect vapor flow or MTS depletion. Regardless of weave geometry, the shapes of the tows remain relatively well-defined and constant during infiltration. Only slight variations and occasional defects destroy this symmetry. Therefore, it seems logical that this simple model designed on the basis of an ideal tow should accurately reflect the changes in surface area during infiltration.

We have demonstrated that high-resolution x-ray tomography can be used to analyze matrix growth quantitatively during CVI. The measured parameters, such as surface-area evolution and pore volume, are of great importance to the validation of process models. The ability to validate experimentally—through direct, noninvasive observation—the predictions of infiltration models will greatly improve our understanding of this technologically important processing route to continuous fiber ceramic-matrix composites.

REFERENCES AND NOTES

1. T. M. Besmann, B. W. Sheldon, R. A. Lowden, D. P. Stinton, *Science* **253**, 1104 (1991).
2. T. M. Besmann, B. W. Sheldon, T. S. Moss III, M. D. Kaster, *J. Am. Ceram. Soc.* **75**, 2899 (1992).
3. R. G. Meisenheimer, personal communication.
4. G. B. Freeman, T. L. Starr, T. C. Elston, *Mater. Res. Soc. Symp. Proc.* **168**, 49 (1990).
5. T. L. Starr, in *Chemical Vapor Deposition of Refractory Metals and Ceramics*, T. M. Besmann, B. M. Gallois, J. Warren, Eds. (Materials Research Society, Pittsburgh, PA, 1992), p. 207.
6. W. D. Carlson and C. Denison, *Science* **257**, 1236 (1992).
7. B. P. Flannery, H. W. Deckman, W. G. Roberge, K. L. D'Amico, *ibid.* **237**, 1439 (1987).
8. U. Bonse *et al.*, *Nucl. Instrum. Methods Phys. Res. A* **246**, 43 (1986).
9. J. H. Kinney, M. C. Nichols, U. Bonse, S. R. Stock, T. M. Breunig, in *Advanced Tomographic Imaging Methods for the Analysis of Materials* (Materials Research Society, Pittsburgh, PA, 1991), vol. 217, p. 81.
10. J. H. Kinney and M. C. Nichols, *Annu. Rev. Mater. Sci.* **22**, 121 (1992).

11. Measurements were made with the XTM on the 31-pole wiggler beam line (BL-10) at Stanford Synchrotron Radiation Laboratory. A double-crystal monochromator [Si(220) reflections] was used for the selection of energies between 20 and 27 keV. High-resolution radiographic images were taken as the sample rotated in 0.5° increments from 0° to 180°. These images were normalized to the incident beam and reconstructed into 3D images with the use of Fourier-filtered back projection.
12. The mass-absorption coefficient for Nicalon was determined by the use of tabulated data from E. F.

- Plechaty *et al.*, in *Tables and Graphs of Photon-Interaction Cross Sections* (Lawrence Livermore National Laboratory, Livermore, CA, 1981), vol 6, rev. 3. The composition of Nicalon was considered to be (by weight) 59% Si, 31% C, and 10% O. A density of 2.6 g cm⁻³ was used for Nicalon.
13. T. M. Breunig, M. C. Nichols, J. H. Kinney, paper presented at the 17th Annual Conference on Composites and Advanced Ceramics, Cocoa Beach, FL, 11 to 15 January 1993.
14. We thank A. M. Gokhale for valuable discussions regarding stereology, A. Gardea for sample preparation, W. Massey for electronics engineering

support, J. Daniel for artwork, and J. Bruner for editorial assistance. Supported by the U.S. Department of Energy (DOE), Advanced Industrial Concepts Materials Program ED38-02, and performed under the auspices of the U.S. DOE by the Lawrence Livermore National Laboratory under contract W-7405-Eng-48 and by Sandia National Laboratories California under Contract DE-AC04-76DP00789; the Stanford Synchrotron Radiation Laboratory is supported by the U.S. DOE, Chemical Sciences Division.

3 December 1992; accepted 23 February 1993

The Nitrogenase FeMo-Cofactor and P-Cluster Pair: 2.2 Å Resolution Structures

Michael K. Chan, Jongsun Kim, D. C. Rees*

Structures recently proposed for the FeMo-cofactor and P-cluster pair of the nitrogenase molybdenum-iron (MoFe)-protein from *Azotobacter vinelandii* have been crystallographically verified at 2.2 angstrom resolution. Significantly, no hexacoordinate sulfur atoms are observed in either type of metal center. Consequently, the six bridged iron atoms in the FeMo-cofactor are trigonally coordinated by nonprotein ligands, although there may be some iron-iron bonding interactions that could provide a fourth coordination interaction for these sites. Two of the cluster sulfurs in the P-cluster pair are very close together (~2.1 angstroms), indicating that they form a disulfide bond. These findings indicate that a cavity exists in the interior of the FeMo-cofactor that could be involved in substrate binding and suggest that redox reactions at the P-cluster pair may be linked to transitions of two cluster-bound sulfurs between disulfide and sulfide oxidation states.

There has been considerable interest in the determination of the structures of the nitrogenase proteins and associated metal centers to learn how nature catalyzes the conversion of N₂ to NH₃ (1). This question has been particularly tantalizing because nitrogenase can fix nitrogen at room temperature, whereas the best industrial process requires both high temperatures and pressures. Nitrogenase consists of two component proteins, the MoFe-protein and Fe-protein that together contain three distinct types of redox centers: two unusual Fe-S clusters, the FeMo-cofactor and the P-cluster pair, located within the MoFe-protein, and a single Fe₄S₄ cluster bound to the Fe-protein. Recently, we proposed structures (designated the "Kim models") for the P-cluster pair and FeMo-cofactor of the nitrogenase MoFe-protein that were based on x-ray diffraction data collected to 2.7 Å resolution (2). The P-cluster pair was described as containing two Fe₄S₄ cubane clusters coupled by two bridging cysteine (Cys) thiols, whereas the FeMo-cofactor was modeled as a dimer of MFe₃S₃ (M = Fe or Mo) partial cubanes linked by three nonprotein ligands. However, alternative models for both centers were subsequently

proposed (3). These alternate models for both the FeMo-cofactor and the P-cluster pair are topologically similar to one another and are based on two MFe₃S₃ (M = Fe or Mo) clusters linked by a common hexacoordinate S.

To definitively characterize the structures of the metal centers, we collected

x-ray diffraction data to 2.2 Å resolution from two *Azotobacter vinelandii* MoFe-protein crystals (2) with a MAR Research imaging plate detector at the Stanford Synchrotron Radiation Laboratory. The images were processed with the MOSFLM and CCP4 packages (4), yielding a final set of 95,078 reflections (90% complete to 2.2 Å resolution, reduced from a total of 258,519 observations with an R_{merge} of 0.136). Refinement of the MoFe-protein model at 2.2 Å resolution with the program X-PLOR (5), followed by TNT (6), has progressed to $R = 0.202$, with root-mean-square (rms) deviations from bond distances and angles of 0.020 Å and 2.98°, respectively. Two types of electron density maps were examined to establish the locations of the metal and S positions in the P-cluster pair (Fig. 1) and FeMo-cofactor (Fig. 2). To define the metal positions, $F_o - F_c$ maps were generated with F_c values calculated from a model that was refined without the metal cofactors and their coordinated ligands. The S positions were then established from $F_o - F_c$ maps with the use of F_c values from a refinement that contained the metal positions but with the cluster S atoms omitted

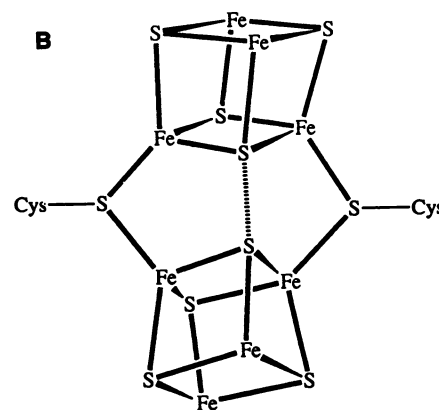
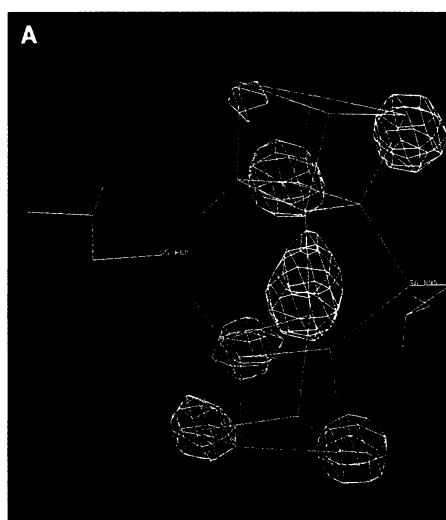


Fig. 1. (A) $F_o - F_c$ difference maps for the P-cluster pair at 2.2 Å resolution. The metal positions are defined in a map generated with the F_c calculated from a model refined without metal centers and coordinated ligands. The magenta contours represent 12 times the standard deviation of this map. The yellow contours define the sulfur positions in a map with F_c calculated from a model refined without the sulfurs. The yellow contours are 6.7 times the standard deviation of this map. (B) Schematic representation of the P-cluster pair in the same orientation as (A).

Division of Chemistry and Chemical Engineering 147-75CH, California Institute of Technology, Pasadena, CA 91125.

*To whom correspondence should be addressed.